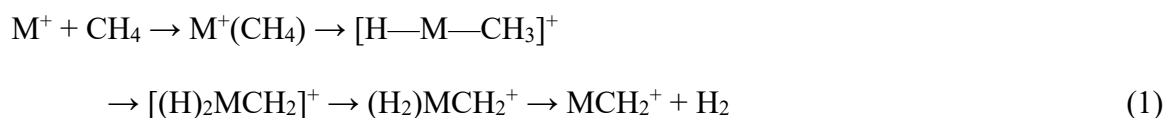


Introduction:

Recently, concerns regarding anthropogenic climate change as a result of greenhouse gas emissions, among other factors, have led to interest in energy source alternatives to coal and oil. One such alternative is natural gas as it is plentiful and cleaner than coal, producing less carbon dioxide and generating more heat per unit mass.^{1,2} However, natural gas poses drawbacks which prevent widespread adoption, such as its volatility at room temperature. Liquefying natural gas for transportation or storage is an energy intensive process and can only be achieved at low temperature and high pressure; this limits the feasibility of its transportation and broader utilization.² In an effort to alleviate this issue, chemists have been searching for a way to convert the major constituent of natural gas, methane, into an easily transportable liquid fuel, such as a heavier hydrocarbon or even methanol. Such a process would allow for easier transportation, expanding the range of uses for methane (by means of its conversion products), such as use in the transportation sector. Furthermore, generating methanol or ethylene from methane would be beneficial as both are precursors to a number of industrial products.²

Methane activation by gas phase transition metals has been investigated as a model for methane catalysis for several decades. Beginning in 1989, Irikura and Beauchamp showed that many third row (5d) transition metal cations (for example Ta⁺, W⁺, Os⁺, Ir⁺, and Pt⁺) spontaneously dehydrogenate methane at room temperature.³⁻⁵ This occurs via a mechanism which first involves the formation of an M⁺(CH₄) entrance channel complex. Then, the metal can insert into a C—H bond to form the [H-M-CH₃]⁺ intermediate. Activation of a second C—H bond produces the [H-M(H)—CH₂]⁺ intermediate, which rapidly rearranges to form the (H₂)MCH₂⁺ exit channel complex. It ultimately releases H₂ and forms the MCH₂⁺ product (reaction 1).³ For 5d M⁺,

sequential reactions with methane form ions up to $[\text{MC}_8\text{H}_{16}]^+$.⁴ This formation of C—C bonds is important in the application of this chemistry as a first step in converting methane into other useful products.



A more complete study by Shayesteh and coworkers in 2009 investigated reactions of 59 atomic metal cations with methane at room temperature in 0.35 Torr of helium.⁶ The study showed methane dehydrogenation by ground state As^+ , Nb^+ , Ta^+ , W^+ , Os^+ , Ir^+ , and Pt^+ according to reaction 1. Additionally, reaction rates for the various metals' dehydrogenation of methane were reported.

The thermodynamics of this reaction provide insight regarding which metals will be observed to dehydrogenate methane at room temperature. Dehydrogenation of methane is endothermic by 455 kJ/mol, thus the resulting metal-ligand interaction must overcome that endothermicity for the reaction to occur at room temperature.⁷ Armentrout compiled data for bond dissociation energies of $\text{M}^+\text{—CH}_2$, which can be used to determine the metal ions which can overcome that endothermicity and dehydrogenate methane at room temperature. Metals with $\text{M}^+\text{—CH}_2$ bond dissociation energies greater than 455 kJ/mol are: Ta^+ , W^+ , Os^+ , Ir^+ , and Pt^+ , consistent with the observation that these metals dehydrogenate methane at close to the collision rate.^{7,8} A value for As^+ was not reported while the reported energy for Nb^+ fell below the 455 kJ/mol threshold, despite its being observed to dehydrogenate methane by Shayesteh et al, albeit at a rate much lower than the collision rate.⁶ In fact, Nb^+ and Zr^+ fall into a category wherein

dehydrogenation of methane is nearly thermoneutral, with reported $M^+—CH_2$ bond dissociation energies of 428 kJ/mol and 447 kJ/mol respectively. Thus, these metals give rise to varied results regarding dehydrogenation of methane. While Shayesteh and coworkers did not observe Zr^+ to dehydrogenate methane, several other studies have seen dehydrogenation of methane by zirconium ions, including one by Armentrout & Sievers and another by Ranasinghe et al.^{6,9,10}

To observe dehydrogenation of methane by Ti^+ and other first row metals, the endothermicity of the reaction must be overcome.¹¹ For these metals, dehydrogenation can still occur with higher collision energy or electronic excitation, which has been observed.¹² An example of a process which overcomes this endothermicity is the sequential addition of multiple methanes. Though not seen for a single methane, activation of methane by Ti^+ is reported by van Koppen et al. to be competitive with adduct formation with the addition of a third methane ligand.^{13,14} In this experiment, the endothermicity is overcome by adding subsequent methane ligands without thermalizing, leading to hot $Ti^+(CH_4)_3$, which can overcome the barriers and endothermicity leading to dehydrogenation. Furthermore, the third methane is found to bind significantly further from the metal center than the first two, which illustrates how dehydrogenation can be competitive with adduct formation. The addition of multiple methane ligands also opens up the opportunity for intermediates beyond metal insertion, such as a dimethyl intermediate as reported by van Koppen and coworkers.¹³

Dehydrogenation of methane by metal ions for which the reaction is endothermic is still possible, as evidenced in various studies discussed previously. A step to better understanding methane activation by these metals is to look at the entrance channel complexes of the form $M^+(CH_4)_n$ ($n=1-4$). The first step to activation of C—H bonds in methane is the weakening of those bonds, which can be visible in the vibrational spectra of these entrance channel complexes as

frequency of vibration is proportional to bond strength. By investigating the shift in stretching frequency of the C—H bonds in these complexes, the weakening of those bonds can be better understood. Furthermore, the geometry of the entrance channel complexes can be deduced, from which further information can be gleaned regarding the potential for subsequent dehydrogenation.

Experimental & Computational Methods:

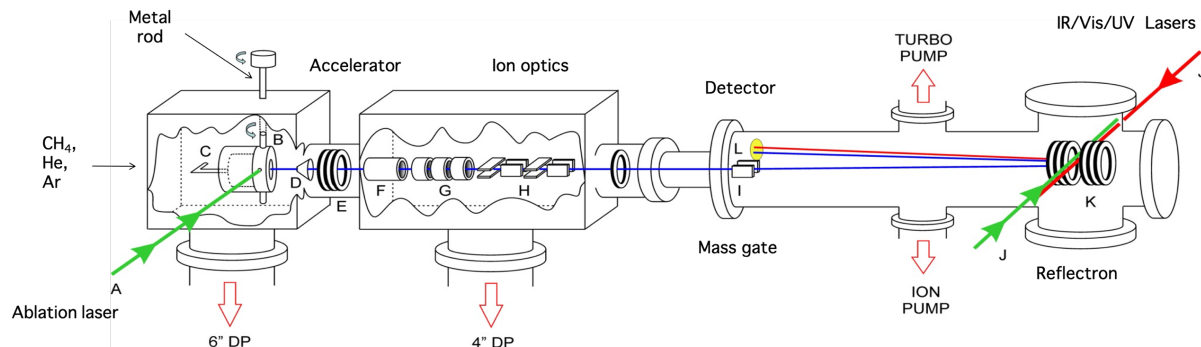


Figure 1: Time-of-flight reflectron mass spectrometer used to take vibrational spectra of the entrance channel complexes.

Experiments are performed on a custom (home-built) dual time-of-flight (TOF) reflectron mass spectrometer and IR laser system, shown in Figure 1. The $M^+(\text{CH}_4)_{1-4}$ ($M=\text{Ti, Zr}$) complexes investigated are produced by laser ablation of a constantly rotating and translating metal rod within the ion source of the instrument. A frequency doubled (532 nm) Nd:YAG laser operated at 7 mJ/pulse and repeating at a 20 Hz repetition rate is used for ablation. A pulsed valve (General Valve, Series 9) is used to introduce a pulse of gas to the ion source just before the ablation laser fires.

A gas composition of 5% CH_4 in He at backing pressure between 80-100 psi is used to produce the $\text{Ti}^+(\text{CH}_4)_n$ complexes. $\text{Ti}^+(\text{CH}_4)(\text{Ar})$ is produced with 0.25% CH_4 and 10% Ar in He at a backing pressure of 80 psi. A gas composition of 0.025-2% CH_4 in He is used for the $\text{Zr}^+(\text{CH}_4)_n$ complexes, while an additional 20-30% Ar in He is used to generate the argon-tagged complexes. Backing pressures for the zirconium complexes ranges from 40 to 80 psi. The major ^{48}Ti and ^{90}Zr isotopes are used for all spectra reported.

Right after being formed, the metal ions pass through an 11 mm long, 2.5 mm ID tube, during which they collide with the CH₄/He/Ar gas mixture, cooling and forming clusters. Subsequently, ions expand into vacuum, further cooling and creating a molecular beam whose rotational temperature is reported to be 15 K.¹⁵ The resultant ion beam is skimmed and extracted into the TOF mass spectrometer where it is accelerated and re-referenced to ground potential. Ions are then mass selected, ensuring only a small band containing the parent ion of interest continue to the reflectron. At the turning point of the reflectron, ions are dissociated by an IR laser system (LaserVision) consisting of a Nd:YAG-pumped optical parametric oscillator/amplifier, producing 7-9 mJ/pulse in the range of investigation (around 3000 cm⁻¹) with a line width of 1.8 cm⁻¹. The wavelength of the laser system is calibrated with the absorption spectrum of methane.¹⁶

Following dissociation, parent and resultant photofragment ions are reaccelerated in the second TOF stage, ultimately hitting a 40 mm dual microchannel plate detector. The flight times of the ions are used to determine their masses. A gated integrator is used to amplify and collect ion signal, which is then recorded by a *LabView* based program. In order to obtain a photodissociation spectrum, fragment signal is first normalized to parent signal, then to laser power as a function of wavelength. The fragments observed correspond to the loss of one or more intact CH₄ in the case of Ti⁺(CH₄)_n (n=2-4) and Zr⁺(CH₄)_n (n=3-4) and the loss of Ar for Ti⁺(CH₄)(Ar) and Zr⁺(CH₄)_n(Ar) (n=1-2).

Corresponding calculations are performed using the *Gaussian09* program package. Optimized geometries for the ions are computed using the B3LYP density functional and the aug-cc-pVTZ basis set. A scaling factor of 0.964 is used in the calculation of vibrational frequencies based on the ratio of experimental and computed values for the stretching frequencies (symmetric and antisymmetric) of bare CH₄. Energies reported include zero-point energies.

Results & Discussion:

The spectra of the entrance channel complexes $M^+(\text{CH}_4)_n$ ($M=\text{Ti, Zr}$; $n=1-4$) are measured by vibrational spectroscopy in the C—H stretching region ($2550-3100\text{ cm}^{-1}$). The smaller complexes are argon-tagged to make $\text{Ti}^+(\text{CH}_4)(\text{Ar})$ and $\text{Zr}^+(\text{CH}_4)_n(\text{Ar})$ ($n=1-2$) in order to take their spectra. This is done because the molecules have to dissociate in order to measure their spectra and the methane binding energy exceeds the photon energy. The laser does make several passes through the ion cloud, so it is possible for the ions to absorb more than one photon. However, for ions this small, infrared multiple-photon dissociation (IRMPD) is inefficient. For clusters with two methanes, IRMPD becomes more efficient, decreasing the necessity of tagging. For larger clusters, the methane binding energy is much smaller, so one photon has enough energy to dissociate the cluster.

The resulting spectra display the C—H stretching frequencies and intensities for these complexes, which reflect how the hydrogens coordinate to the metal. This coordination occurs between two extremes: η^2 in which two hydrogens coordinate to the metal resulting in C_{2v} symmetry for an $M^+(\text{CH}_4)$ complex and a metal carbon to furthest hydrogen bond angle $\angle M-C-H$ of $\sim 124^\circ$; and η^3 where $\angle M-C-H=180^\circ$, demonstrating C_{3v} symmetry.

Potential Energy Surfaces

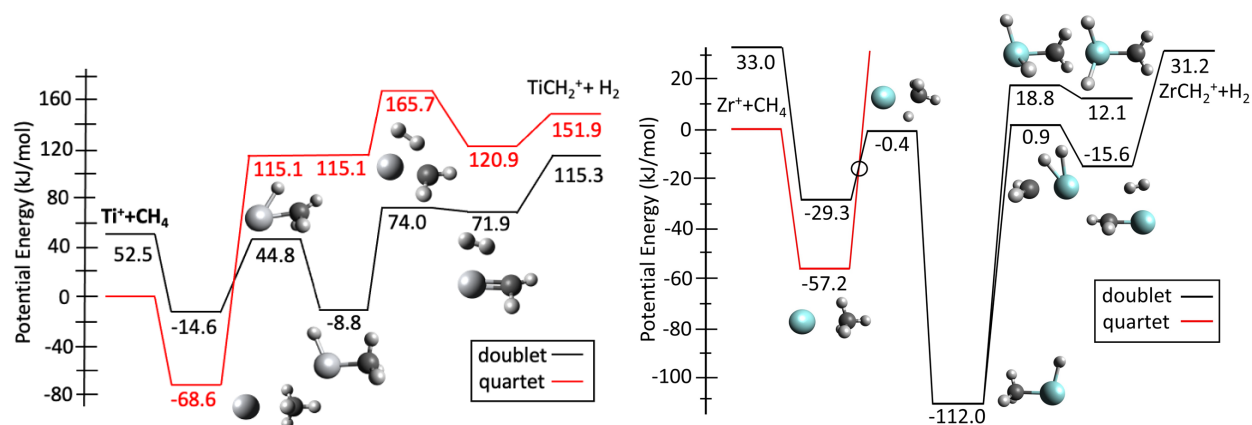


Figure 2: High-spin (red) and low-spin (black) potential energy surfaces for the reaction of Ti^+ and Zr^+ with CH_4 at the B3LYP/aug-cc-pVTZ level of theory. Lowest energy geometries shown.

The potential energy surfaces for the reactions of Ti^+ and Zr^+ with methane are shown in Figure 2. In both cases, the ground state of the reactants and the entrance channel complex $\text{M}^+(\text{CH}_4)$ is high-spin. Both surfaces show a significant C—H bond activation barrier for the formation of an $[\text{H—M—CH}_3]^+$ insertion intermediate. Additionally, in both cases for the transition state and all further intermediates and products, the lowest energy pathway is lower spin than the reactants.

One major difference that can be noted between Ti^+ and Zr^+ is that the latter makes stronger covalent bonds, leading to a much more stable insertion intermediate (-112.0 kJ/mol for Zr^+ versus -8.8 kJ/mol for Ti^+). Another difference is the overall endothermicity of the reaction to form the $\text{MCH}_2^+ + \text{H}_2$ products, being endothermic by 115.3 kJ/mol for Ti^+ and only by 31.2 kJ/mol for Zr^+ . The potential energy surfaces calculated here are similar to those calculated by Russo & Sicilia for Ti^+ and by Armentrout & Sievers for Zr^+ .^{9,11} It bears noting that the experimentally determined $\text{Zr}^+—\text{CH}_2$ bond dissociation energy of 447 kJ/mol combined with the experimental 455 kJ/mol

endothermicity for the dehydrogenation of methane suggests methane dehydrogenation by zirconium should only be endothermic by about 8 kJ/mol.⁶⁻⁸ This indicates theory may overpredict the endothermicity of this pathway. It should also be noted that under our experimental conditions, we expect formation of only the high-spin $M^+(\text{CH}_4)$ ($M=\text{Ti}, \text{Zr}$) entrance channel complexes.

$\text{Ti}^+(\text{CH}_4)_n$

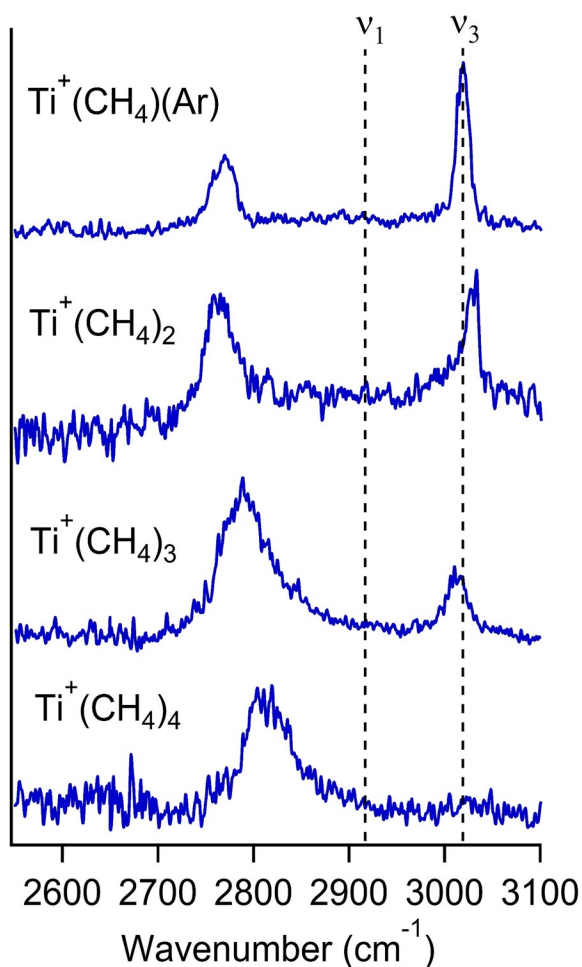


Figure 3: Experimental vibrational spectra of $\text{Ti}^+(\text{CH}_4)(\text{Ar})$ and $\text{Ti}^+(\text{CH}_4)_n$ ($n=2-4$) in the C—H stretching region (2550-3100 cm^{-1}) plotted as normalized photofragment yield versus wavenumber. The symmetric (ν_1) and antisymmetric (ν_3) stretches for bare methane are indicated by dashed vertical lines.

Experimental spectra of $\text{Ti}^+(\text{CH}_4)_n$ are shown in Figure 3, displaying peaks red shifted from the symmetric C—H stretch in bare methane (2917 cm^{-1}). A second peak at 3000 cm^{-1} , close to the CH_4 antisymmetric stretch (3019 cm^{-1}), decreases in intensity with the addition of methanes, completely disappearing for the $n=4$ complex. This is indicative of the methane binding orientation changing as the number of methanes in the complex increases.

Table 1: Experimental and calculated binding energies of $\text{Ti}^+(\text{CH}_4)(\text{Ar})$ and $\text{Ti}^+(\text{CH}_4)_n$ ($n=1-4$)

Species	Calculated cm^{-1}	Calculated kJ/mol	Experimental (kJ/mol)
$\text{Ti}^+\text{---CH}_4$	5746	68.7	70.3 ± 2.5
$\text{Ti}^+\text{CH}_4\text{---Ar}$	2578	30.8	
$\text{Ti}^+\text{CH}_4\text{---CH}_4$	4968	59.4	72.8 ± 2.5
$\text{Ti}^+(\text{CH}_4)_2\text{---CH}_4$	1183	14.2	27.6 ± 6.3
$\text{Ti}^+(\text{CH}_4)_3\text{---CH}_4$	1779	21.3	41.0 ± 3.3

Calculations are at 0 K at the B3LYP/aug-cc-pVTZ level of theory. Experimental results Ref 13

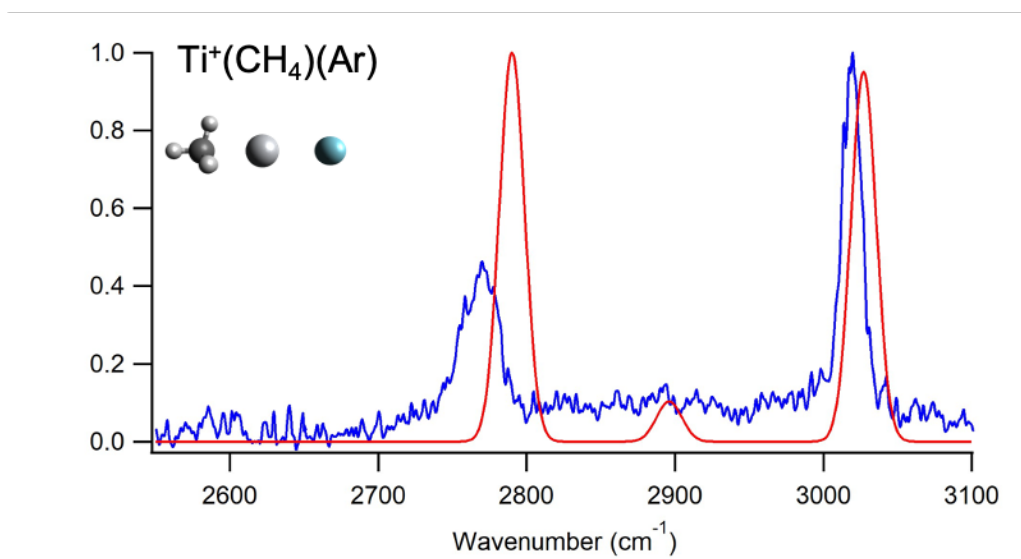


Figure 4: Experimental photodissociation spectrum (blue), simulated spectrum (red), and the optimized geometry of $\text{Ti}^+(\text{CH}_4)(\text{Ar})$ at the B3LYP/aug-cc-pVTZ level of theory.

As a result of its high calculated binding energy of 5746 cm^{-1} (Table 1), $\text{Ti}^+(\text{CH}_4)$ requires more than one photon to dissociate. The inefficiency of IRMPD for molecules this small resulted in a low dissociation yield for $\text{Ti}^+(\text{CH}_4)$. For the argon-tagged complex, $\text{Ti}^+(\text{CH}_4)(\text{Ar})$, the argon tag is calculated to have a binding energy of 2578 cm^{-1} . The spectrum for the argon-tagged complex (Figure 4) has improved signal to noise, but has similar features to the untagged spectrum, showing a moderately-intense peak at 2770 cm^{-1} and a more intense peak at 3020 cm^{-1} .

Our calculations, at B3LYP/aug-cc-pVTZ, predict the $\text{Ti}^+(\text{CH}_4)$ molecule to have η^3 methane hydrogen coordination with a Ti—C distance $r_{\text{Ti}-\text{C}}=2.350 \text{ \AA}$. The calculated binding energy for $\text{Ti}^+(\text{CH}_4)$ is 68.7 kJ/mol , in agreement with the experimental value of $70.3 \pm 2.5 \text{ kJ/mol}$.¹³ For $\text{Ti}^+(\text{CH}_4)(\text{Ar})$, our calculations predict the Ar—Ti—C atoms to be collinear and η^3 methane hydrogen coordination ($\angle \text{Ti}-\text{C}-\text{H}=180^\circ$). The Ti—C bond length for the argon-tagged complex is calculated to be 2.365 \AA , a minimal difference from the untagged complex. The calculated peak

positions for the C—H stretches do not change significantly (≤ 4 cm^{-1} shifts) between the tagged and untagged complexes, demonstrating that the argon-tag only minimally affects the spectrum. It should also be noted that both complexes, as with Ti^+ , have a quartet ground state.

Three peaks appear in the simulated spectrum: two of relatively equal intensity at 2789 and 3029 cm^{-1} and one very weak peak at 2895 cm^{-1} . The peak at 2789 cm^{-1} is representative of the symmetric stretch of the C—H closest to the metal. The peak at 3029 cm^{-1} corresponds to the free distal C—H stretch. The peak at 2895 cm^{-1} in the simulated spectrum arises from two weak antisymmetric C—H stretches; it does not appear in the experimental spectrum. The peaks that do appear in the experimental spectrum (2770 and 3020 cm^{-1}) are fairly sharp and slightly red shifted from the predicted peaks.

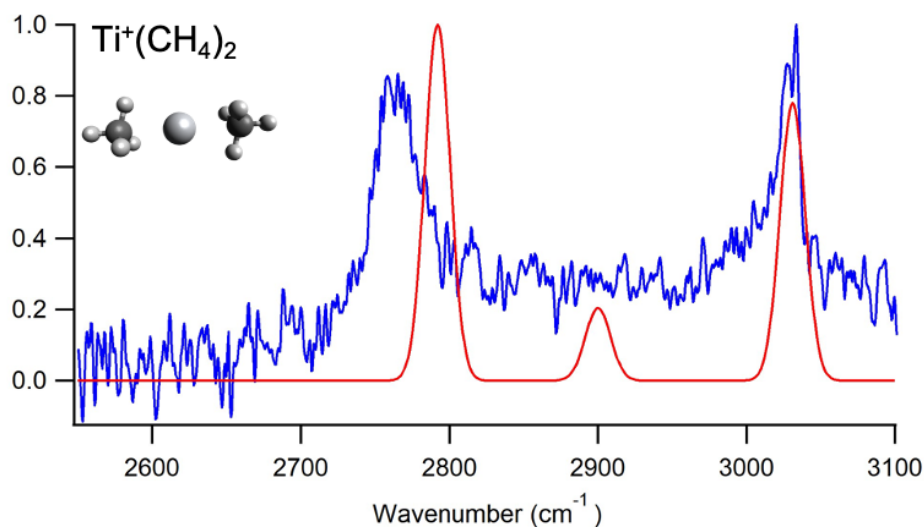


Figure 5: Experimental photodissociation spectrum (blue), simulated spectrum (red), and the optimized geometry of $\text{Ti}^+(\text{CH}_4)_2$ at the B3LYP/aug-cc-pVTZ level of theory.

Despite the predicted binding energy of 4968 cm^{-1} for the second methane, $\text{Ti}^+(\text{CH}_4)_2$ readily dissociates. There are two intense peaks in the experimental spectrum (Figure 5) at 2765 and 3034 cm^{-1} . Calculations predict collinear C—Ti—C atoms and equal Ti—C bond lengths of 2.370 \AA . The optimized geometry has C_{2h} symmetry with η^3 hydrogen coordination for both methanes, whose hydrogens are staggered by 60° . Two intense peaks in the simulated spectrum, representative of the symmetric proximate C—H stretch and the free distal C—H stretch, appear at 2790 and 3031 cm^{-1} respectively. There is a third, much weaker peak at 2900 cm^{-1} , corresponding to two antisymmetric C—H stretches. While there is no matching peak in the experimental spectrum, a baseline above zero in this region indicates some dissociation is occurring. While the predicted position for the symmetric stretch peak is 25 cm^{-1} too high, the predicted peak for the free C—H stretch aligns well with the experimental spectrum.

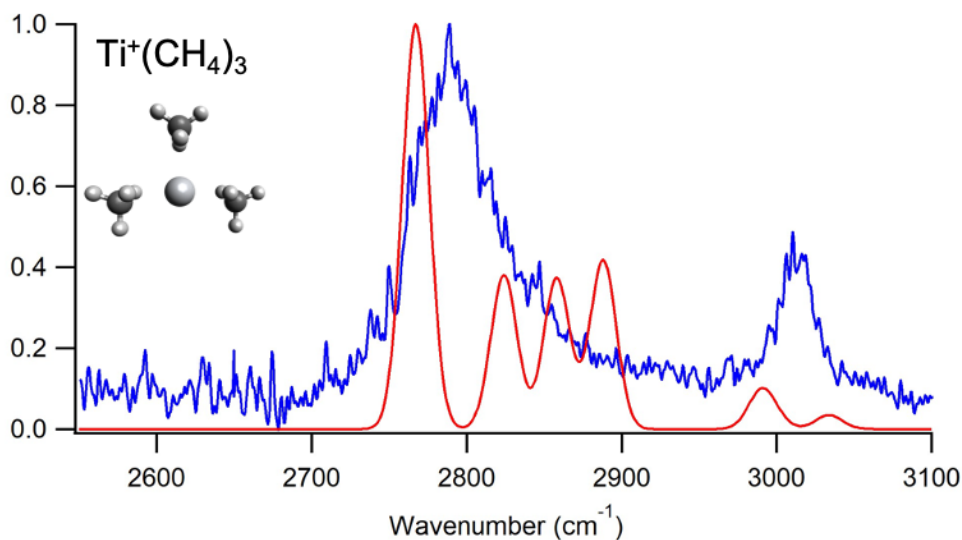


Figure 6: Experimental photodissociation spectrum (blue), simulated spectrum (red), and the optimized geometry of $\text{Ti}^+(\text{CH}_4)_3$ at the B3LYP/aug-cc-pVTZ level of theory.

Calculations predict a binding energy of 1183 cm^{-1} for the third methane, much weaker than the first two ligands. The experimental spectrum for $\text{Ti}^+(\text{CH}_4)_3$ (Figure 6) displays an intense, broad peak centered at 2789 cm^{-1} and another, narrower peak with lower intensity at 3010 cm^{-1} . The optimized structure for $\text{Ti}^+(\text{CH}_4)_3$ displays C_{2v} symmetry with two methanes equidistant from the metal at $r_{\text{Ti}-\text{C}}=2.480\text{ \AA}$ and the third methane at a distance of 2.731 \AA . The first two methanes exhibit hydrogen coordination between η^2 and η^3 , with $\angle\text{Ti}-\text{C}-\text{H}=150^\circ$ while the third methane has η^2 coordination ($\angle\text{Ti}-\text{C}-\text{H}=125^\circ$). An intense peak appears in the simulated spectrum at 2766 cm^{-1} , arising from the symmetric proximate C—H stretches of the two close methanes, while the corresponding peak for the further methane appears at 2824 cm^{-1} . The antisymmetric C—H stretch peaks appear at 2848 and 2887 cm^{-1} for the close and distant methanes, respectively. The low intensity peaks at 2989 and 3034 cm^{-1} result from the distal C—H stretches. In contrast to the highly resolved simulated spectrum, the experimental spectrum does not display separate peaks for the close and distant methanes. Instead, one broad peak appears in the region of the symmetric proximate C—H stretches, and a narrow peak appears for the distal C—H stretches. This likely arises due to a dynamic structure in which the three methanes interconvert rapidly over a small barrier.

Although dehydrogenation of methane has been reported upon the addition of a third methane, it is not observed here.^{13,14} It is likely this channel was the result of incomplete cooling as the first two methanes are added, leading to the addition of the third methane to produce very hot $\text{Ti}^+(\text{CH}_4)_3$, which can dehydrogenate. Loss of H_2 is endothermic for $\text{Ti}^+(\text{CH}_4)_3$ and due to higher pressure in our source, there are more collisions resulting in $\text{Ti}^+(\text{CH}_4)_3$ that is too cool to react.

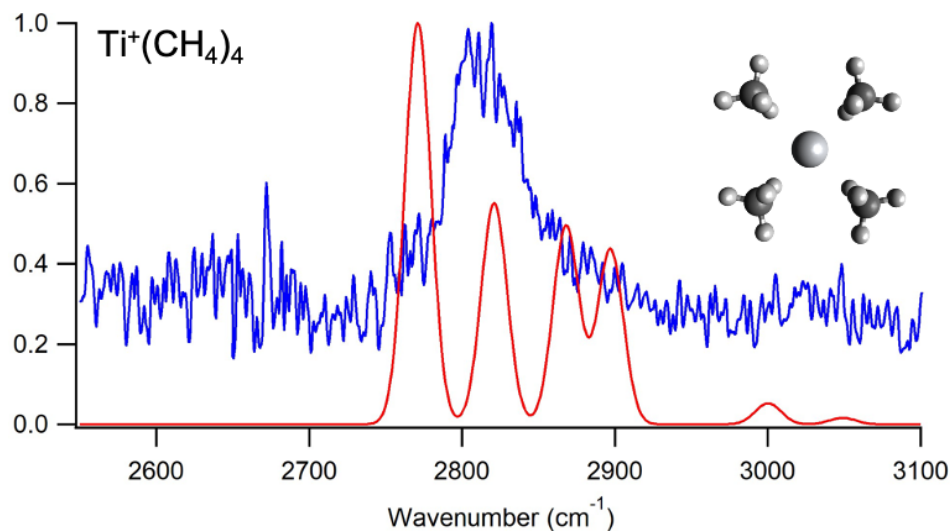


Figure 7: Experimental photodissociation spectrum (blue), simulated spectrum (red), and the optimized geometry of $\text{Ti}^+(\text{CH}_4)_4$ at the B3LYP/aug-cc-pVTZ level of theory.

The fourth methane has a calculated binding energy of 1779 cm^{-1} , somewhat stronger than the third methane, which is consistent with previous studies.¹³ The experimental spectrum measured for $\text{Ti}^+(\text{CH}_4)_4$ (Figure 7) exhibits a single, intense, broad peak at 2810 cm^{-1} . The optimized geometry from calculations predicts a distorted square planar structure consisting of two methanes with Ti—C bond lengths of 2.558 \AA and two methanes at 2.721 \AA . All four methanes are predicted to have η^2 methane hydrogen coordination; this accounts for the absence of a peak near 3000 cm^{-1} . The simulated spectrum predicts peaks from the proximate C—H stretches at 2771 and 2820 cm^{-1} for the near and distant methanes, respectively. The predicted peaks for the antisymmetric C—H stretches appear at 2867 and 2896 cm^{-1} . As with $\text{Ti}^+(\text{CH}_4)_3$, the experimental spectrum consists of a single, broad peak likely due to dynamic structure, wherein the near and distant methanes interconvert rapidly over a low energy barrier. These titanium complexes are also discussed in our paper comparing structures of methane complexes of titanium and vanadium.¹⁷

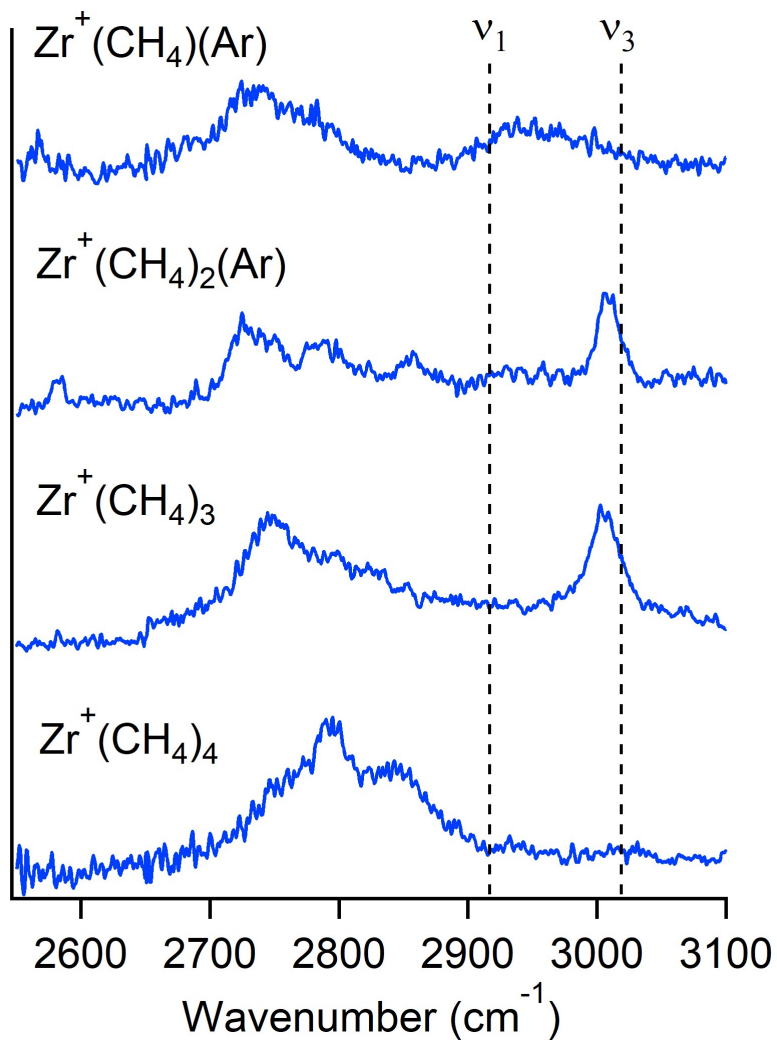


Figure 8: Experimental vibrational spectra of $\text{Zr}^+(\text{CH}_4)_n(\text{Ar})$ $n=1-2$ and $\text{Zr}^+(\text{CH}_4)_n$ $n=3-4$ in the C—H stretching region ($2550-3100 \text{ cm}^{-1}$) plotted as normalized photofragment yield versus wavenumber. The symmetric (ν_1) and antisymmetric (ν_3) stretches for bare methane are indicated by dashed vertical lines.

Experimental spectra of $\text{Zr}^+(\text{CH}_4)_n$ are shown in Figure 8. As with the titanium complexes, these spectra show peaks red shifted from the symmetric and antisymmetric C—H stretches in bare methane (2917 and 3019 cm^{-1} , respectively). The peak representative of the symmetric stretch,

amplified and red shifted by the weakening of the proximate C—H bonds due to binding to the metal, appears around 2730 cm⁻¹ for the smaller clusters and shifts to higher wavenumbers with increasing size of the complex. Another peak, near the antisymmetric stretch for bare methane, appears for the n=1-3 clusters, but disappears in the n=4 spectrum, indicative of a change in the coordination of the ligands to the metal as the number of ligands increases.

Table 2: Experimental and calculated binding energies of Zr⁺(CH₄)_n(Ar) (n=1-2) and Zr⁺(CH₄)_n (n=1-4)

Species	Calculated cm ⁻¹	Calculated kJ/mol
Zr ⁺ —CH ₄	4782	57.2
Zr ⁺ CH ₄ —Ar	2488	29.8
Zr ⁺ CH ₄ —CH ₄	4902	58.6
Zr ⁺ (CH ₄) ₂ —Ar	133	1.6
Zr ⁺ (CH ₄) ₂ —CH ₄	1171	14.0
Zr ⁺ (CH ₄) ₃ —CH ₄	2043	24.4

Calculations are at 0 K at the B3LYP/aug-cc-pVTZ level of theory.

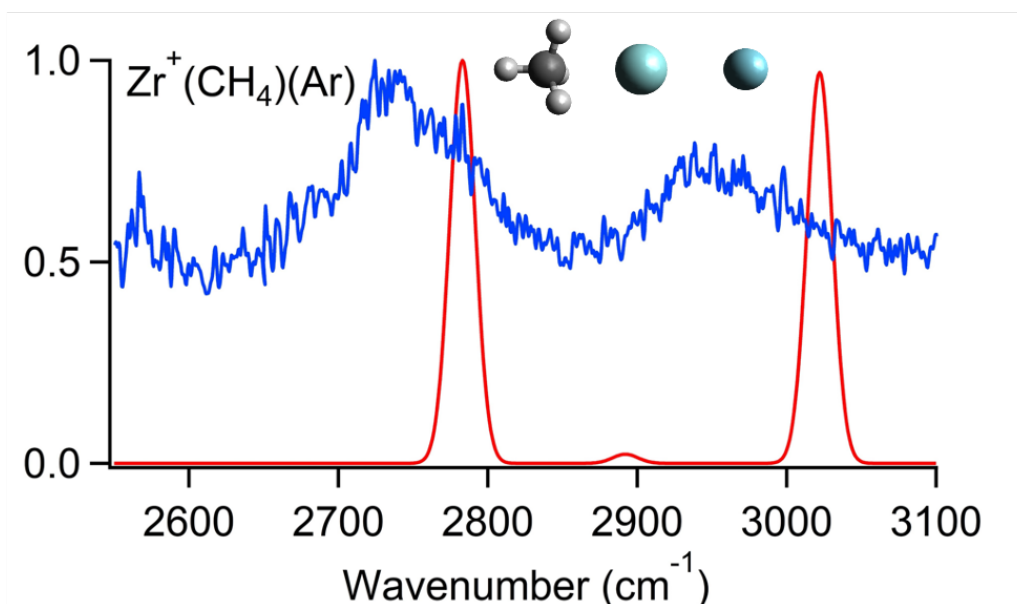


Figure 9: Experimental photodissociation spectrum (blue), simulated spectrum (red), and the optimized geometry of $\text{Zr}^+(\text{CH}_4)(\text{Ar})$ at the B3LYP/aug-cc-pVTZ level of theory.

As with titanium, the relatively high binding energy of 4782 cm^{-1} for $\text{Zr}^+(\text{CH}_4)$ (Table 2) means it must be argon-tagged in order to obtain a spectrum. The experimental spectrum for $\text{Zr}^+(\text{CH}_4)(\text{Ar})$ (Figure 9) exhibits broad peaks around 2730 and 2950 cm^{-1} . These are red shifted from the peaks in the simulated spectrum at 2783 and 3022 cm^{-1} for the symmetric proximate and free distal C—H stretches, respectively.

Calculations for the optimized geometry for $\text{Zr}^+(\text{CH}_4)(\text{Ar})$ predict the Ar—Zr—C atoms to be collinear, with η^3 methane hydrogen coordination. The Zr—C bond length is predicted to be 2.590 \AA , a distance of 0.011 \AA longer than is calculated for the untagged complex. The simulated peak positions for the tagged and untagged spectra are similar, less than 6 cm^{-1} shifts, demonstrating that the argon tag has a minimal effect on the spectrum.

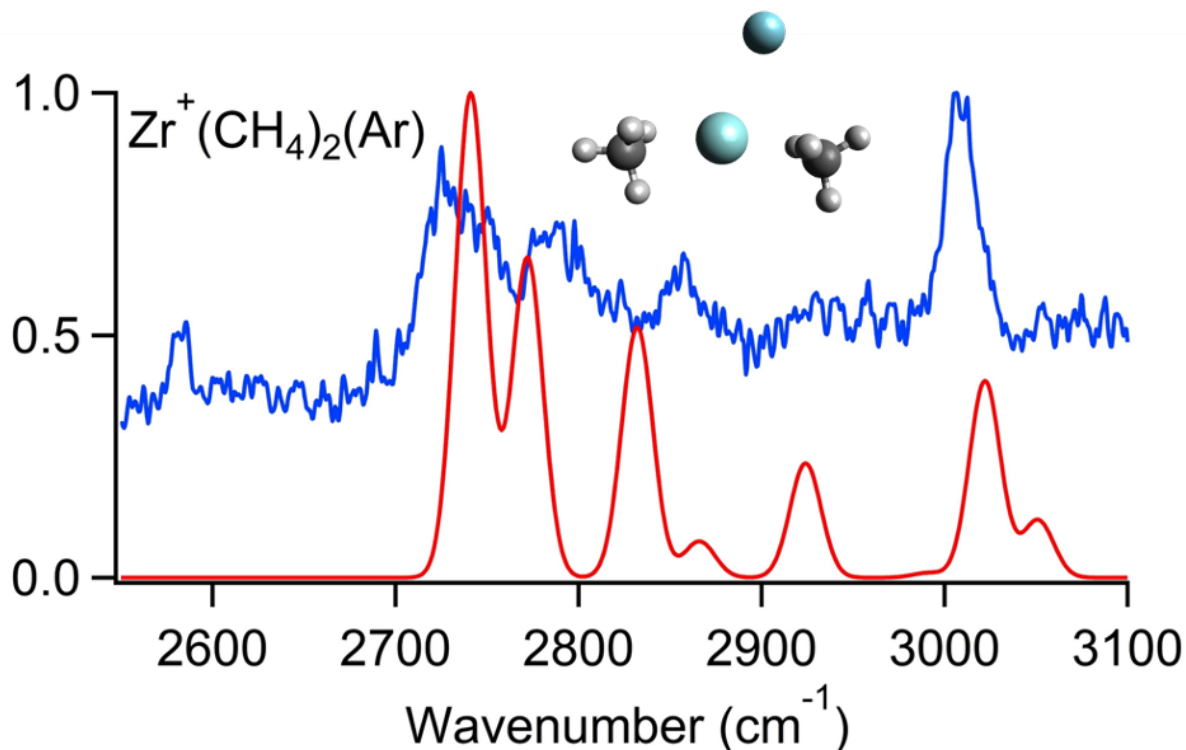


Figure 10: Experimental photodissociation spectrum (blue), simulated spectrum (red), and the optimized geometry of $\text{Zr}^+(\text{CH}_4)_2(\text{Ar})$ at the B3LYP/aug-cc-pVTZ level of theory.

Due to the high binding energy of the second methane, 4902 cm^{-1} (Table 2), argon-tagging is again necessary to obtain the experimental spectrum for the two-methane complex. There are a number of peaks present in the experimental spectrum for $\text{Zr}^+(\text{CH}_4)_2(\text{Ar})$ at 2582 , 2725 , 2783 , 2857 , and 3006 cm^{-1} (Figure 10). While the C—Zr—C atoms are calculated to be collinear in the untagged molecule, the addition of an argon-tag bends $\angle\text{C—Zr—C}$ to 161° . The $\angle\text{C—Zr—Ar}$ are 79.8 and 119.4° with the methane further from the argon tag displaying almost η^3 coordination ($\angle\text{C—Zr—H} = 171^\circ$; $r_{\text{Zr—C}} = 2.527\text{ \AA}$) and the other methane closer to η^2 ($\angle\text{C—Zr—H} = 139^\circ$; $r_{\text{Zr—C}} = 2.654\text{ \AA}$).

The series of predicted peaks in the simulated spectrum (Figure 10) are a result of the symmetry of the molecule being perturbed by the argon tag. The η^2 and η^3 methanes are differently

red shifted, leading to unique C—H stretches and peaks in the spectrum. The simulated spectrum predicts peaks at 2740 and 2772 cm^{-1} for the symmetric proximate C—H stretch for the η^2 and η^3 methanes, respectively. The small peak at 2582 cm^{-1} is likely due to the $(\text{H}_2)\text{ZrCH}_2^+(\text{CH}_4)$ exit channel complex. This is discussed in detail in our paper on the zirconium complexes.¹⁸

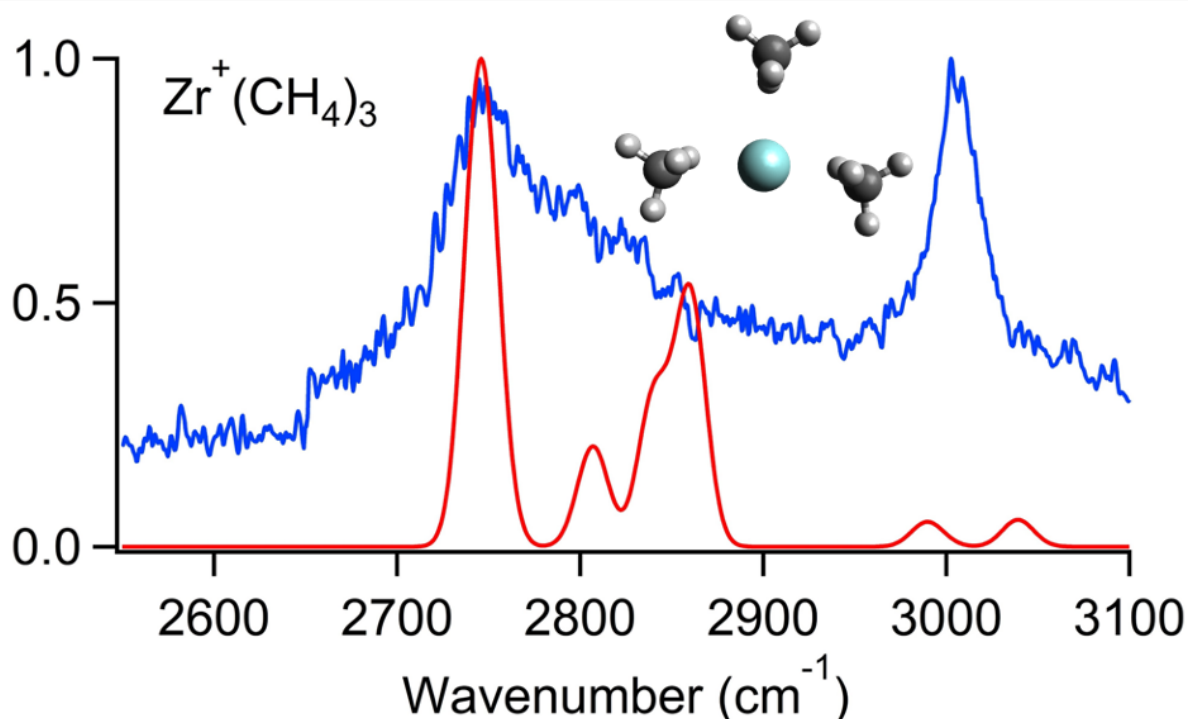


Figure 11: Experimental photodissociation spectrum (blue), simulated spectrum (red), and the optimized geometry of $\text{Zr}^+(\text{CH}_4)_3$ at the B3LYP/aug-cc-pVTZ level of theory.

The lower binding energy of the third methane of 1171 cm^{-1} means the molecule readily dissociates to allow us to obtain an experimental spectrum for $\text{Zr}^+(\text{CH}_4)_3$ (Figure 11). The spectrum exhibits two intense peaks: a broad peak centered around 2747 cm^{-1} and a sharper peak at 3002 cm^{-1} . The optimized geometry for the molecule is nearly C_{2v} , exhibiting two methane binding orientations. One methane is η^2 with a Zr—C bond length of 2.866 Å, while the other two are

nearly η^2 ($\angle\text{Zr—C—H} = 143^\circ$; $r_{\text{Zr—C}} = 2.637 \text{ \AA}$). The $\angle\text{C—Zr—C}$ bond angles are 96° with the η^2 methane and 167° between the nearly η^2 methanes. The breadth of the lower wavenumber peak in the experimental spectrum and its tailing to higher energies suggests that the methanes interconvert rapidly.

The simulated spectrum predicts peaks for the symmetric C—H stretch of the nearly η^2 methanes (2746 cm^{-1}) and the η^2 methane (2806 cm^{-1}). The antisymmetric C—H stretches are predicted to be at 2840 cm^{-1} for the nearly η^2 methanes and 2860 cm^{-1} for the η^2 methane. Weak peaks in the simulated spectrum arise from the nearly η^2 methanes at 2990 and 3039 cm^{-1} , accounting for the distal symmetric and antisymmetric C—H stretches, respectively.

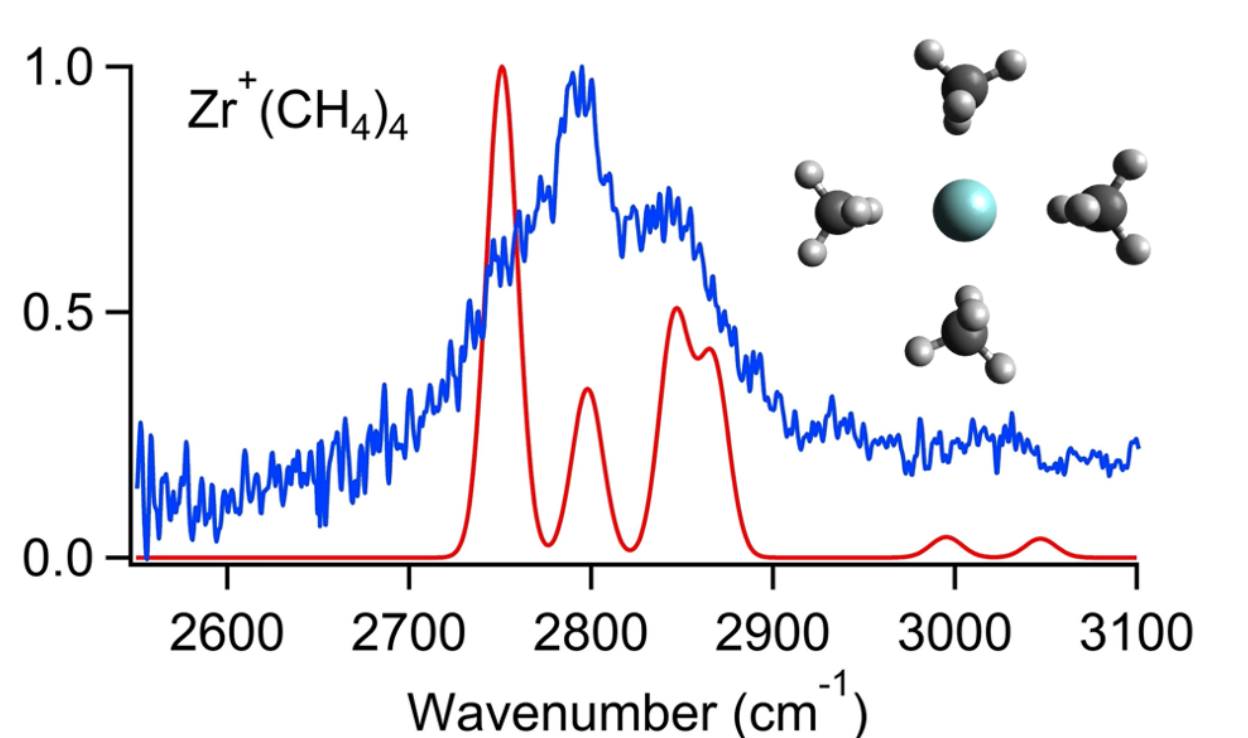


Figure 12: Experimental photodissociation spectrum (blue), simulated spectrum (red), and the optimized geometry of $\text{Zr}^+(\text{CH}_4)_4$ at the B3LYP/aug-cc-pVTZ level of theory.

The fourth methane is calculated to be more strongly bound than the third, with a binding energy of 2043 cm⁻¹ (Table 2), similar to the trend observed in the titanium complexes. The reasoning for this lies in the loss of s-d hybridization of the first two methanes, which is shared between the third and fourth methane. Two clear peaks appear in the experimental spectrum for Zr⁺(CH₄)₄ (Figure 12): a more intense peak at 2795 cm⁻¹ and another, less intense peak at 2834 cm⁻¹.

Zr⁺(CH₄)₄ is predicted to have a slightly distorted square planar geometry, similar to the Ti⁺(CH₄)₄ complex, where methanes bind with η² coordination with ∠C—Zr—C bond angles between 89 and 90°. The calculated bond lengths predict two closer methanes at r_{Zr—C}=2.679 Å and two further methanes at 2.844 Å. The closer methanes are predicted to be bent away from the metal with ∠Zr—C—H bond angles of 135° (rather than the characteristic 124° for η² coordination).

Peaks for the symmetric C—H stretches in the simulated are predicted to be at 2751 and 2798 cm⁻¹ for the near and far methanes, respectively, while the antisymmetric stretches show up at 2847 and 2865 cm⁻¹, respectively. A true square planar structure for this molecule is predicted to be a transition state 129 cm⁻¹ above the distorted square planar minimum. This low barrier suggests that intermediate structures may also contribute to the experimental spectrum, leading to the higher absorption observed near 2770 cm⁻¹. The absence of a peak near 3000 cm⁻¹ in the experimental spectrum indicates that structures with η³ methane hydrogen coordination are not contributing to the spectrum.

Ti⁺(CH₄)_n vs. Zr⁺(CH₄)_n

Figures 3 and 8 show the experimental spectra of the entrance channel complexes of the reactions of Ti⁺ and Zr⁺ with methane. Comparing peak positions, the M⁺(CH₄)_n complexes for n=1-2 exhibit similar peaks for M=Ti and M=Zr. Although these complexes are predicted to have similar binding energies, the spectra for the Zr⁺ complexes exhibit broader peaks than the corresponding Ti⁺ spectra. The symmetric C—H stretches for these complexes occur at similar energies between the two metals, with peak positions within 15 cm⁻¹ of each other. Moving to the n=3 complexes, these too appear similar for titanium and zirconium, with the exception that the C—H symmetric stretch for Zr⁺(CH₄)₃ appears 42 cm⁻¹ more red shifted than in Ti⁺(CH₄)₃. The M⁺(CH₄)₄ complexes also exhibit similar spectra as they both lack peaks near 3000 cm⁻¹, indicating fully η² methane hydrogen coordination. The Zr⁺ peak, however, is a resolved doublet showing contributions from the symmetric and antisymmetric proximate C—H stretches, while the Ti⁺ spectrum shows only a single, broad peak.

The geometries of the analogous entrance channel complexes of M⁺(CH₄)_n for titanium and zirconium are similar. For both metals, the M⁺(CH₄)(Ar) and M⁺(CH₄)₂ complexes demonstrate η³ methane hydrogen coordination with the metal, carbons, and argon for the tagged complexes all collinear. For both n=2 complexes, the methane molecules are staggered by 60°. Moving to the M⁺(CH₄)₃ complexes, both titanium and zirconium exhibit geometries with two methanes with shorter bond lengths to the metal with coordination between η² and η³ and a third methane further from the metal with η² coordination. The experimental spectra for the complexes of both metals are consistent with rapid interconversion of the methanes, demonstrating broad peaks rather than the well-defined peaks predicted in the simulated spectra. Finally, the n=4 complexes of both

metals adopt distorted square planar structure, with two distinct bond lengths and η^2 coordination. The breadth of the peaks in the experimental spectra indicate that the methanes interconvert in both complexes, however the resolution of two peaks in the proximate C—H stretching region for $\text{Zr}^+(\text{CH}_4)_4$ suggests slower interconversion than for $\text{Ti}^+(\text{CH}_4)_4$.

Summary & Conclusions:

Vibrational spectroscopy on entrance channel complexes of the form $M^+(CH_4)_n$ ($M=Ti, Zr$; $n=1-4$) in the C—H stretching region ($2550-3100\text{ cm}^{-1}$) combined with simulated spectra based on calculations at the B3LYP/aug-cc-pVTZ level of theory elucidate the structure of these complexes. The vibrational spectra are obtained by photofragment spectroscopy, monitoring for the loss of argon for tagged complexes and loss of methane for untagged complexes.

The resulting spectra exhibit peaks due to the symmetric and free distal C—H stretches of methane. The titanium complexes demonstrate symmetric stretches red shifted by 149, 152, 128, and 107 cm^{-1} for $n=1-4$, respectively, relative to $\nu_1 = 2917\text{ cm}^{-1}$ in bare methane. The zirconium complexes demonstrate symmetric stretches red shifted by 187, 192, 170, and 122 cm^{-1} for $n=1-4$, respectively, again relative to ν_1 in bare methane. This red shifting is indicative of a weakening of the C—H bond, the first step in methane activation. For both metals, the methane has η^3 hydrogen coordination in the smaller entrance channel complexes ($n=1-2$) with $n=3$ demonstrating a combination of η^3 and η^2 coordination. Both $Ti^+(CH_4)_4$ and $Zr^+(CH_4)_4$ exhibit all η^2 coordination. The symmetric stretch of proximate C—H bonds in η^2 methane are more red shifted than those due to η^3 methane. A peak near 3000 cm^{-1} in the spectra is representative of the distal C—H bond stretching, which is intense for η^3 complexes and disappears for η^2 coordination and thus is not present in the $n=4$ spectra.

References:

- (1) N. Cavaliere, V.; J. Mindiola, D. Methane: A New Frontier in Organometallic Chemistry. *Chem. Sci.* **2012**, *3* (12), 3356–3365. <https://doi.org/10.1039/C2SC20530K>.
- (2) Webb, J. R.; Bolaño, T.; Gunnoe, T. B. Catalytic Oxy-Functionalization of Methane and Other Hydrocarbons: Fundamental Advancements and New Strategies. *ChemSusChem* **2011**, *4* (1), 37–49. <https://doi.org/10.1002/cssc.201000319>.
- (3) Irikura, K. K.; Beauchamp, J. L. Osmium Tetroxide and Its Fragment Ions in the Gas Phase: Reactivity with Hydrocarbons and Small Molecules. *J. Am. Chem. Soc.* **1989**, *111* (1), 75–85. <https://doi.org/10.1021/ja00183a014>.
- (4) Irikura, K. K.; Beauchamp, J. L. Methane Oligomerization in the Gas Phase by Third-Row Transition-Metal Ions. *J. Am. Chem. Soc.* **1991**, *113* (7), 2769–2770. <https://doi.org/10.1021/ja00007a070>.
- (5) Irikura, K. K.; Beauchamp, J. L. Electronic Structure Considerations for Methane Activation by Third-Row Transition-Metal Ions. *J. Phys. Chem.* **1991**, *95* (21), 8344–8351. <https://doi.org/10.1021/j100174a057>.
- (6) Shayesteh, A.; Lavrov, V. V.; Koyanagi, G. K.; Bohme, D. K. Reactions of Atomic Cations with Methane: Gas Phase Room-Temperature Kinetics and Periodicities in Reactivity. *J. Phys. Chem. A* **2009**, *113* (19), 5602–5611. <https://doi.org/10.1021/jp900671c>.
- (7) Armentrout, P. B. Methane Activation by 5 d Transition Metals: Energetics, Mechanisms, and Periodic Trends. *Chem. – Eur. J.* **2017**, *23* (1), 10–18. <https://doi.org/10.1002/chem.201602015>.
- (8) Armentrout, P. B. Guided Ion Beam Studies of Transition Metal–Ligand Thermochemistry. *Int. J. Mass Spectrom.* **2003**, *227* (3), 289–302. [https://doi.org/10.1016/S1387-3806\(03\)00087-3](https://doi.org/10.1016/S1387-3806(03)00087-3).
- (9) Armentrout, P. B.; Sievers, M. R. Activation of CH₄ by Gas-Phase Zr⁺ and the Thermochemistry of Zr–Ligand Complexes. *J. Phys. Chem. A* **2003**, *107* (22), 4396–4406. <https://doi.org/10.1021/jp027820d>.
- (10) Ranasinghe, Y. A.; MacMahon, T. J.; Freiser, B. S. Formation of Thermodynamically Stable Dications in the Gas Phase by Thermal Ion-Molecule Reactions: Tantalum(2+) and Zirconium(2+) with Small Alkanes. *J. Phys. Chem.* **1991**, *95* (20), 7721–7726. <https://doi.org/10.1021/j100173a032>.
- (11) Sicilia, E.; Russo, N. Theoretical Study of Ammonia and Methane Activation by First-Row Transition Metal Cations M⁺ (M = Ti, V, Cr). *J. Am. Chem. Soc.* **2002**, *124* (7), 1471–1480. <https://doi.org/10.1021/ja0112487>.
- (12) Hendrickx, M.; Ceulemans, M.; Gong, K.; Vanquickenborne, L. Theoretical Study on the Stability of Low-Spin Hydridomethyl Complexes of the First-Row Transition Metal Cations. *J. Phys. Chem. A* **1997**, *101* (13), 2465–2470. <https://doi.org/10.1021/jp962754z>.
- (13) van Koppen, P. A. M.; Perry, J. K.; Kemper, P. R.; Bushnell, J. E.; Bowers, M. T. Activation of Methane by Ti⁺: A Cluster Assisted Mechanism for σ -Bond Activation, Experiment, and Theory *Int. J. Mass Spectrom.* **1999**, *185–187*, 989–1001. [https://doi.org/10.1016/S1387-3806\(98\)14269-0](https://doi.org/10.1016/S1387-3806(98)14269-0).
- (14) Van Koppen, P. A. M.; Kemper, P. R.; Bushnell, J. E.; Bowers, M. T. Methane Dehydrogenation by Ti⁺: A Cluster-Assisted Mechanism for σ -Bond Activation. *J. Am. Chem. Soc.* **1995**, *117* (7), 2098–2099. <https://doi.org/10.1021/ja00112a026>.

- (15) Kocak, A.; Austein-Miller, G.; Pearson, W. L.; Altinay, G.; Metz, R. B. Dissociation Energy and Electronic and Vibrational Spectroscopy of $\text{Co}^+(\text{H}_2\text{O})$ and Its Isotopomers. *J. Phys. Chem. A* **2013**, *117* (6), 1254–1264. <https://doi.org/10.1021/jp305673t>.
- (16) Gordon, I. E.; et al. The HITRAN2016 Molecular Spectroscopic Database. *J. Quant. Spectrosc. Radiat. Transf.* **2017**, *203*, 3–69. <https://doi.org/10.1016/j.jqsrt.2017.06.038>.
- (17) Kozubal, J.; Heck, T.; Metz, R. B. Structures of $\text{M}^+(\text{CH}_4)_n$ ($\text{M}=\text{Ti}, \text{V}$) Based on Vibrational Spectroscopy and Density Functional Theory. *J. Phys. Chem.* Accepted
- (18) Kozubal, J.; Heck, T.; Metz, R. B. Vibrational Spectroscopy of Intermediates and C–H Activation Products of Sequential Zr^+ Reactions with CH_4 . *J. Phys. Chem. A* **2020**, *124* (40), 8235–8245. <https://doi.org/10.1021/acs.jpca.0c07027>.